Draft version June 22, 2022
Typeset using LaTeX **twocolumn** style in AASTeX63

Rejuvenated accretors have less bound envelopes: Impact of the first Roche lobe overflow on the common envelope in gravitational wave progenitors

M. Renzo ■ [other and order TBD] ■,[1] K. Breivik,[1] R. Farmer,[2] E. Zapartas,[3,4,1] M. Lau,[3,4,1] S. Justham,[5,6] and B. D. Metzger[7,1]

[1] *Center for Computational Astrophysics, Flatiron Institute, New York, NY 10010, USA*
[2] *Max-Planck-Institut für Astrophysik, Karl-Schwarzschild-Straße 1, 85741 Garching, Germany*
[3] *School of Physics and Astronomy, Monash University, Clayton, Victoria 3800, Australia*
[4] *OzGrav: The ARC Centre of Excellence for Gravitational Wave Discovery, Australia*
[5] *Anton Pannekoek Institute of Astronomy and GRAPPA, University of Amsterdam, Science Park 904, 1098 XH Amsterdam, The Netherlands*
[6] *School of Astronomy and Space Science, University of the Chinese Academy of Sciences, Beijing 100012, PR China*
[7] *Columbia Astrophysics Laboratory, Columbia University, New York, New York 10027, USA*

ABSTRACT

Common envelope (CE) evolution is an outstanding open problem in stellar evolution, critical to the formation of compact binaries including gravitational-wave (GW) sources. In the "classical" isolated binary evolution scenario for double compact objects, the CE is usually the second mass transfer phase. Thus, the donor star of the CE is the product of a previous binary interaction, often a stable Roche lobe overflow (RLOF). Because of the accretion of mass during the first RLOF, the main-sequence core of the accretor star grows and is "rejuvenated". This modifies the core-envelope boundary region and decreases significantly the envelope binding energy for the remaining evolution. Comparing accretor stars from self-consistent binary models to stars evolved as single, we demonstrate that the rejuvenation can lower the energy required to eject a CE by $\sim 4-58\%$ for both black hole and neutron star progenitors, depending on the evolutionary stage and final orbital separation. Therefore, GW progenitors experiencing stable mass transfer may more easily survive subsequent possible CE events compared to current predictions. Despite their high mass, our accretors also experience extended "blue loops" , which may have observational consequences for low-metallicity stellar populations and asteroseismology.

Keywords: stars: massive – stars: binaries: mass transfer – stars: binaries: common envelope – stars: binaries: accretors

1. INTRODUCTION

Common envelope (CE) is an important evolutionary channel for massive isolated binaries to become gravitational-wave (GW) sources, despite recent debates on its relevance for the progenitors of the most massive binary black holes (e.g., van den Heuvel et al. 2017; Pavlovskii et al. 2017; Klencki et al. 2020, 2021; van Son et al. 2021; Marchant et al. 2021). CE remains a crucial step in the formation, among many other compact binaries, of cataclysmic variable (e.g., Paczynski 1976), double white dwarfs (e.g., Zorotovic et al. 2010; Korol et al. 2017; Kremer et al. 2017; Renzo et al. 2021; Thiele et al. 2021), binary neutron stars (NS, e.g., Vigna-Gómez et al. 2018, 2020), merging black hole-neutron stars (e.g., Kruckow et al. 2018; Broekgaarden & Berger 2021) and possibly low-mass binary black holes (BH, e.g., Dominik et al. 2012; van Son et al. 2021).

In the "classical scenario" for binary BHs and/or NSs (e.g., Tutukov & Yungelson 1993; Belczynski et al. 2016; Tauris et al. 2017), the progenitor binary experiences a first dynamically stable mass transfer through Roche lobe overflow (RLOF) between two non-compact stars. Subsequently, the initially more massive RLOF-donor collapses to a compact object without disrupting the binary (e.g., Blaauw 1961; Renzo et al. 2019). Only afterwards, as the initially less massive RLOF-accretor expands, a second mass-transfer phase occurs and is typically dynamically unstable, that is a CE (e.g., Dominik et al. 2012; Belczynski et al. 2016; Kruckow et al. 2018). This second mass transfer is responsible for the orbital shrinking (Paczynski 1976) allowing the system to merge

within the age of the Universe. Therefore, in this scenario, the donor star of the CE is the former accretor of the first RLOF (e.g., Klencki et al. 2020; Law-Smith et al. 2020; Renzo & Gotberg 2021).

The first stable RLOF typically occurs during the main sequence of the initially less massive star and accretion modifies its structure (e.g., Neo et al. 1977; Packet 1981; Blaauw 1993; Cantiello et al. 2007; Renzo & Gotberg 2021). On top of the enrichment of the envelope with CNO-processed material from the donor star core (Blaauw 1993; Renzo & Gotberg 2021; El-Badry et al. 2022), and the substantial spin-up, accretors are expected to adjust their core-size to the new mass in a "rejuvenation" process (e.g., Neo et al. 1977; Hellings 1983, 1984). The readjustment is driven by mixing at the boundary between the convective core and the envelope, which refuels the convective region of hydrogen (H). This mixing also affects the thermal structure of the partially H-depleted layer above the helium (He), which we refer to as core-envelope boundary layer (CEB). It is in the CEB that the density rises and most of the envelope binding energy is accumulated for the remaining stellar lifetime. Consequently, the success or failure of the CE ejection, and the final separation are likely decided in the CEB layer (e.g., Ivanova et al. 2013, 2020), and may be different depending on whether the CE-donor accreted mass previously or not.

Here, we use structure and evolution binary models to study the impact of the first RLOF phase on the outcome of possible subsequent CE events. Sec. 2 describe our `MESA` calculations. In Sec. 3 we show the ratio of binding energies of our accretor models divided single stars of the same total post-RLOF mass. We discuss our findings and conclude in Sec. 4. Appendix A presents a proof-of-principle numerical experiment illustrating the effect of changing the core-envelope boundary region and the and rotation on the envelope binding energy, and Appendixes B–D present additional plots.

2. PRE-COMMON ENVELOPE EVOLUTION

We use `MESA` (version 15140, Paxton et al. 2011, 2013, 2015, 2018, 2011) to compute the evolution of binaries which experience mass transfer after the end of the donor's main sequence, that is case B Roche lobe overflow (RLOF, Kippenhahn & Weigert 1967). Our output files are compatible for use in the population synthesis code `POSYDON` (Fragos et al. 2022) and publicly available together with our input files and customized routines at doi:10.5281/zenodo.6600641. Our setup is similar to Renzo & Gotberg (2021), except for the metallicity: here we adopt $Z = 0.0019 \simeq Z_{\odot}/10$, relevant for the progenitor population of GW events (e.g., van Son et al. 2021). Moreover, we apply throughout the star a small amount of mixing with diffusivity `min_D_mix`=100. This improves the numerical stability by smoothing properties across adjacent cells, without introducing significant quantitative variations, and is a typical numerical technique used in asteroseismology calculations (J. Fuller, private comm.).

We adopt initial period $P = 100\,\mathrm{days}$ and choose initial masses $(M_1, M_2) = (18, 15), (20, 17), (38, 30)\,M_{\odot}$. We focus on the initially less massive stars, which after accretion become $M_2 = 15 \rightarrow 18, 17 \rightarrow 20, 30 \rightarrow 36\,M_{\odot}$, roughly representative of NS, uncertain core-collapse outcome, and BH progenitors, respectively. However, we emphasize that the core-collapse outcome (NS or BH formation, with explosion or not), cannot be decided solely based on the (total or core) mass of a star (e.g., O'Connor & Ott 2011; Farmer et al. 2016; Patton & Sukhbold 2020; Zapartas et al. 2021; Patton et al. 2022).

Our `MESA` models assume that the accretion efficiency is limited by rotationally enhanced wind mass loss (e.g., Sravan et al. 2019; Wang et al. 2020a; Renzo & Gotberg 2021; Sen et al. 2022). However, this may lead to less conservative mass transfer than suggested by observations (e.g., Wang et al. 2021, see also Renzo & Gotberg 2021).

After the binary detaches from the Roche lobe (see discussion in Renzo & Gotberg 2021), our simulations artificially detach[1] the stars and continue the evolution of the accretor as a single star until it reaches carbon depletion (defined by central carbon mass fraction $X_{\rm c}(^{12}\mathrm{C}) < 2 \times 10^{-4}$). This reduces the complexity and computing time by avoiding to simulate the late evolutionary phases of the RLOF-donors, and implies that we neglect further possible – but not expected in this regime – mass transfer episodes (case BB RLOF, Laplace et al. 2020) and tidal interactions between the stars. We also neglect the impact of the SN ejecta with the accretor (e.g., Hirai et al. 2018; Ogata et al. 2021) and the orbital consequences of the RLOF-donor core-collapse (e.g., Brandt & Podsiadlowski 1995; Kalogera 1996; Tauris & Takens 1998; Renzo et al. 2019).

To illustrate the physical reason why the first RLOF may influence the envelope structure of the accretor much later on, we also compute comparison stars. For each mass, we compute non-rotating single stars with otherwise identical setup, and "engineered" stars which we modify at terminal age main sequence (TAMS, cen-

[1] We make the routine to detach a `MESA` binary on-the-fly publicly available https://github.com/MESAHub/mesa-contrib/

tral hydrogen mass fraction $X_c(^1H) < 10^{-4}$) to mimic crudely the impact of rejuvenation of the accretors CEB (see also Appendix A).

At the onset of a CE event, the photospheric radius $R \equiv R_{RL,donor}$ is the size of the Roche lobe of the donor star determined by the binary separation and mass ratio (e.g., Paczyński 1971; Eggleton 1983). Thus, we compare the internal structure of accretors to single and engineered stars at various epochs defined by a fixed photospheric radius $R = 100,\ 200,\ 300,\ 500,\ 1000\,R_\odot$.

3. ACCRETORS FROM SELF-CONSISTENT BINARY MODELS

Fig. 1 shows the evolution of our binaries on the Hertzsprung-Russell (HR) diagram. The thin dashed lines show the evolution of the donor stars (see also, e.g., Yoon 2017; Götberg et al. 2017, 2018; Laplace et al. 2020; Laplace et al. 2021) from ZAMS, through RLOF, until our definition of detachment. The solid lines correspond to the full evolution of the accretors, from zero age main sequence (ZAMS), through RLOF, until carbon depletion. The high luminosity excursion during the main sequence of the accretors corresponds to the dip in luminosity of the donor during RLOF (see e.g., Renzo & Gotberg 2021). During this phase the accretor is progressively spun-up, and accretes CNO-processed material from the donor's inner layers which are mixed downwards in the envelope by meridional circulations and thermohaline mixing, and its core is rejuvenated because of the increased mass (see also Sravan et al. 2019; Renzo & Gotberg 2021; Wang et al. 2020a). During the brief RLOF phase, our accretors grow to $M_2 = 15 \rightarrow 18, 17 \rightarrow 20, 30 \rightarrow 36\,M_\odot$, respectively, corresponding to an overall mass transfer efficiency $\beta_{RLOF} = |\Delta M_{accretor}/\Delta M_{donor}| = 0.29,\ 0.30,$ and 0.43, respectively (see discussion in Renzo & Gotberg 2021).

All three accretor models experience a blueward evolution after beginning to ascend the Hayashi track. In the two lowest mass models, this results in a blue-loop, which last $\sim 10^5$ years. These models spend a significant fraction of their He core burning as hot yellow/blue supergiants, and reach $\log_{10}(T_{eff}/[K]) \gtrsim 4.2$. Our most massive accretor ($M_2 = 30 \rightarrow 36\,M_\odot$) evolves towards hotter temperatures during core He burning, but never fully recovers closing the blue loop. Its excursion to hottest temperatures occurs after He core depletion and lasts $\sim 10^4$ years.

Blue loops are not expected for single stars with $M \gtrsim 12\,M_\odot$ (e.g., Walmswell et al. 2015), and their occurrence is known to be sensitive to the He profile above the H-burning shell, and specifically the mean molecular weight profile (Walmswell et al. 2015; Farrell et al. 2022). Thus it is not surprising that RLOF-accretion, which modifies the CEB, may lead to blue loops, and formation of yellow-supergiants (e.g., Dorn-Wallenstein et al. 2020). We note that comparison single stars also experience a late blue-ward evolution, but not a "loop" back to red. This behavior is likely related to the relatively high wind mass-loss rate assumed (see Renzo et al. 2017), and the models with initial mass $\gtrsim 30\,M_\odot$ are qualitatively similar to the most massive accretor in Fig. 1 even without accreting matter from a companion: the occurrence of blue loops is notoriously sensitive to many single star physics uncertainties, and while they appear consistently in our accretor models, their physicality should be tested further.

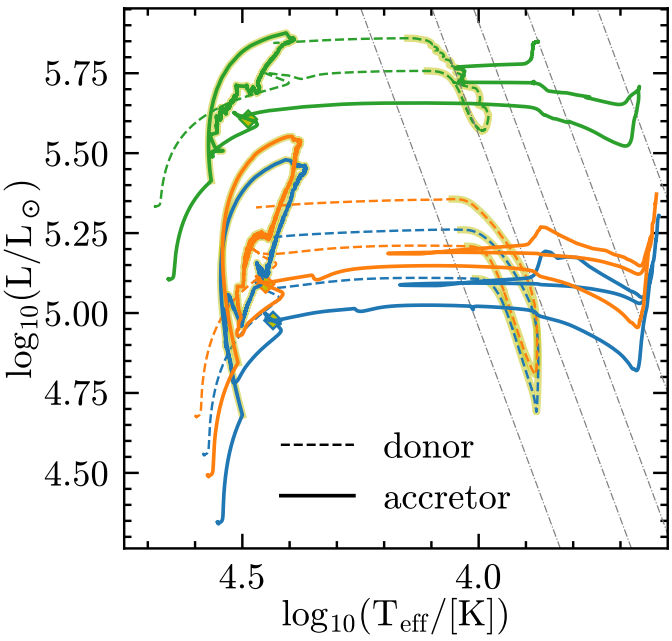

Figure 1. HR diagram of the binary systems. The thin dashed lines show the evolution of the donors until RLOF detachment, the solid lines show the accretors from ZAMS, through RLOF accretion (marked by a yellow outline), until core carbon depletion. Yellow diamonds mark the accretor's TAMS (not shown for donor). The thin dot-dashed lines mark constant radii of $R = 100, 200, 300, 500, 1000\,R_\odot$, all models have $Z = 0.0019$, period 100 days, and initial masses of 38 and $30\,M_\odot$ (green), 20 and $17\,M_\odot$ (orange), 18 and $15\,M_\odot$ (blue).

However, in the context of GW progenitors, blue loops are not crucial since they correspond to a decrease in radius, which would not result in binary interactions during the loop. They might change the mass-loss history of the accretor, but since they occur in a short evolutionary phase, their impact should be limited.

Fig. 2 shows the specific entropy (s) profile – which determines the thermo-dynamical properties of the stars –

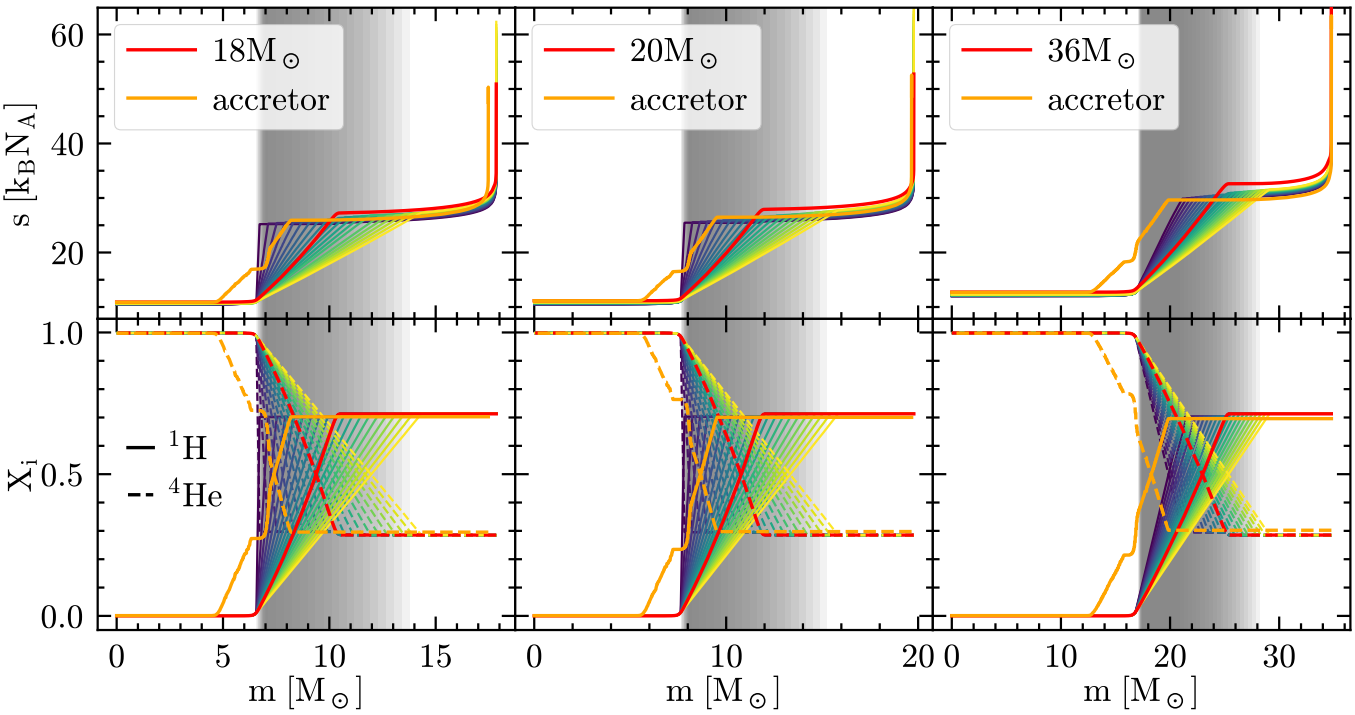

Figure 2. Specific entropy s (top row), H (bottom row, solid lines), and He (bottom row, dashed lines) TAMS profiles for non-rotating single stars (red), accretors (orange), and "engineered" models of the same total mass as the post-RLOF mass of the accretors. The overlapping gray bands emphasize the CEB region, which is well defined at TAMS.

and the H and He mass fractions at TAMS for our accretor models (orange), single non-rotating stars (red) and "engineered" models of roughly same total mass as the accretor post-RLOF. A gray region highlights the CEB (roughly corresponding to H mass fraction $X_c(^1\mathrm{H}) + 0.01 < X(^1\mathrm{H}) < X_{\rm surf}(^1\mathrm{H}) - 0.01$, with X_c and $X_{\rm surf}$ the central and surface value of the hydrogen mass fraction), and their overlap produces the shade in Fig. 2. We compare our models at the same total post-RLOF mass ($M \simeq M_2$) because it enters in Eq. 1 and is typically used in rapid population synthesis codes to construct accretors from single star models (e.g., Hurley et al. 2002). We present in Fig. 9 a comparison between TAMS profiles of accretors, single stars, and engineered models with the same *initial* mass as an alternative comparison that should bracket the range of sensible comparison models.

Accretion through RLOF affects the CEB layer in more subtle ways than we impose in our "engineered" models. One expects the CEB in accretors to be steeper than in a star evolving as single, resulting in models qualitatively more similar to our engineered models with the steeper entropy and composition in the CEB (darker lines in Fig. 2-3, Fig. 6, and Fig. 9–10). In fact, rejuvenation of the accretor is caused by an increase in mass coordinate of the convective core (and consequent refueling of H in the core): this is a thermal process related to convection and convective boundary mixing. Since the convective turnover timescale in the core of a massive star is shorter than (*i*) the nuclear timescale – over which the composition of the core changes, (*ii*) the donor thermal timescale – governing case B RLOF mass-transfer, and (*iii*) the accretor thermal timescale – governing the thermal readjustment of the star, the increase in mass coordinate of the core should create a steep composition and entropy gradient at the new (post-accretion) outer edge. In practice, binary interactions occur after a finite amount of the accretor's main-sequence has elapsed. This pre-RLOF duration depends on the period and mass ratio of the two stars. For our binaries with initial $P = 100$ days and $q = M_2/M_1 \simeq 0.8$, RLOF starts after $\sim$ 10, 9, and 5 Myrs from the least massive to the most massive binary, which correspond to central H mass fractions $X_c(^1\mathrm{H}) = 0.27, 0.23$, and 0.21 for the accretors. Thus, the accreting stars are not homogeneous in composition at the onset of RLOF: the convective core is already bound by a composition gradient that generally impedes the mixing (e.g., Yoon & Langer 2005). Thus, the advance in mass coordinate of the convective region due to mass accretion (i.e., the "rejuvenation process") during RLOF occurs against a gradient (of entropy, μ, H, and He) set by the pre-RLOF evolution.

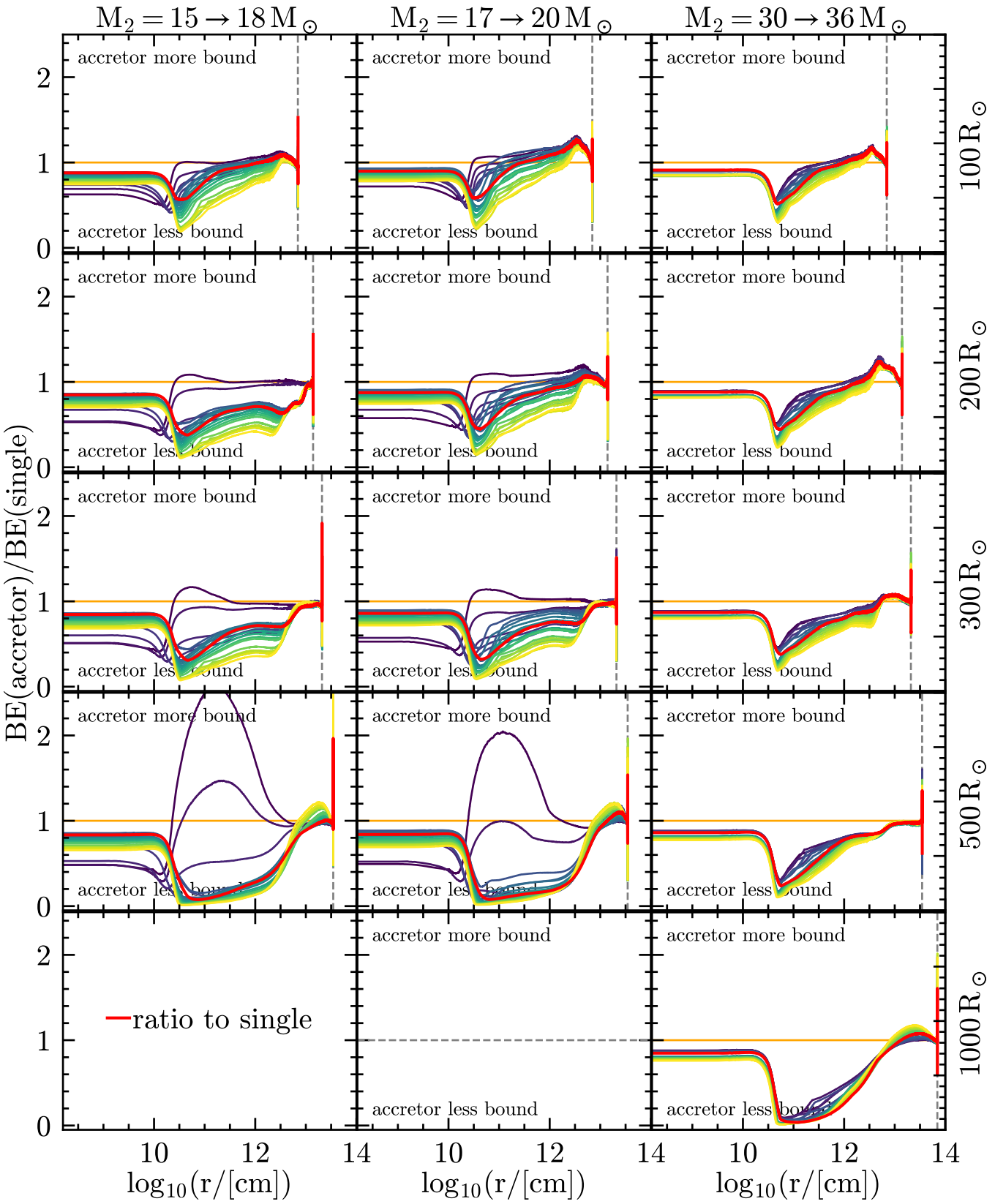

Figure 3. Ratios of the binding energy profiles (including internal energy) of the accretor stars divided stars of the same total mass post-RLOF. The orange solid line at 1 shows the ratio of the accretor to itself as a sanity check, red solid lines show the ratio of the accretor to a non-rotating single star, while the other colors show the ratio to "engineered" star. Each panel shows the ratios at the first time the models reach the radius indicated on the right and by the vertical dashed gray line. For the binding energy profiles in the numerator and denominator see Fig. 8.

To quantify the impact of the first RLOF phase on the outcome of the second mass transfer phase, we evolve forward all the TAMS profiles shown in Fig. 2 and compare them at fixed outer radii. In the "classical" binary evolution path, after the RLOF-donor collapses to a compact object, the evolutionary expansion of the RLOF-accretor triggers a CE. Physically, the CE outcome is determined by the thermal and dynamical reaction of the now-shared envelope to the inspiraling binary (e.g., Ivanova et al. 2013, 2020; Renzo et al. 2021). However, a common oversimplification is to rely on energy conservation ("$\alpha_{\rm CE}\lambda_{\rm CE}$ algorithm", e.g., Webbink 1984; de Kool 1990) to determine CE ejection and final separation, therefore, we focus here on the RLOF-accretor/CE-donor binding energy profile. We calculate the cumulative binding energy outside mass coordinate m as (e.g., de Kool 1990; Dewi & Tauris 2000; Lau et al. 2022):

$$BE(m,\alpha_{\rm th}) = -\int_m^M dm' \left(-\frac{Gm'}{r(m')} + \alpha_{\rm th} u(m')\right) \quad , \tag{1}$$

with $r(m')$ radius, $u(m')$ the internal energy of a shell of mass thickness dm' and outer Lagrangian mass coordinate m', and G the gravitational constant. The integral domain goes from mass coordinate m, which can be thought of the mass of the "core" surviving a hypothetical CE, to the surface. The parameter $0 \leq \alpha_{\rm th} \leq 1$ is the fraction of internal energy (including recombination energy) that can be used to lift the shared CE. It is possible that $\alpha_{\rm th}$ may not be constant during a CE (e.g., if recombination happens in already unbound material it cannot contribute to the CE energetics) or across binary systems entering a CE at different evolutionary stages. For $\alpha_{\rm th} = 0$, Eq. 1 give the gravitational binding energy (dashed lines in Fig. 6-7), while $\alpha_{\rm th} = 1$ assumes perfectly fine-tuned use of all the internal energy (solid lines, Klencki et al. 2020). These two cases bracket the range of possible use of internal energy to eject the CE. We checked that the additional inclusion of the rotational energy in Eq. 1 contributes to less than $\lesssim 10\%$ of the cumulative binding energy only in the outermost layers – likely to be crossed during a dynamical plunge-in in CE evolution – and for $R \lesssim 300\,R_\odot$ – afterwards, even the accretor spin down significantly.

Because of the large range of BE across the stellar structures, it is hard to appreciate directly the magnitude of the effect of RLOF-driven rejuvenation on the BE profile (shown in Fig. 8). Figure 3 presents the ratio of the local value of the cumulative binding energy from the surface of our accretor models divided the comparison single stars, as a function of radius. The two lowest mass accretors (left and central column) do not expand to $R = 1000\,R_\odot$ before carbon depletion. To compute the ratio, we interpolate linearly the single star models on the mesh of our accretor, using the fractional Lagrangian mass coordinate m/M as independent coordinate. We calculate these ratio when both the stars reach for the first time radii $R = 100, 200, 300, 500, 1000\,R_\odot$ (see vertical gray dashed lines), corresponding to the assumed Roche lobe radius of the donor at the onset of the CE.

In each panel, radial coordinates r for which the lines in Fig. 3 are below one correspond to radii at which the accretor models are less bound than the comparison single star or engineered model. For $R \lesssim 300 R_\odot$, the outermost layers (more likely to be crossed by the binary during the dynamical plunge-in phase of the CE) may be slightly less bound in single stars than accretors (red line greater than 1). But for most of the envelope radius, the ratio is smaller than one, suggesting it would take less energy to eject the outer layers of the envelope of the accretors down to such r. All of our accretor models, regardless of them being NS or BH progenitor, and regardless of their evolutionary phase are qualitatively more similar to the darker lines representing engineered models with steeper CEB profiles.

The minimum ratio of binding energies occur roughly at the inner edge of the CEB layer in Fig. 3. Considering the ratio to single stars (red lines), the minima range between 0.56-0.07; 0.58-0.08; and 0.51-0.04 from our least to most massive binary. In other words, at the radius where the difference between accretors and single stars models is largest, which is also the location where the outcome of a common envelope is likely to be decided (e.g., Ivanova et al. 2013), the accretor's binding energy is roughly between $\sim 50 -$ few% of the binding energy of a single star. Regardless of the mass, the larger the outer radius the smaller the minimum of the ratio of binding energies: the differences caused by RLOF accretion and rejuvenation of the core grows as the stars evolve and their core contract.

Defining the He core boundary as the outermost location where $X < 0.01$ and $Y > 0.1$, we can fix $m = M_{\rm He}$ in Eq. 1 to obtain an integrated binding energy for the envelope:

$$BE_{\rm env} \equiv BE(m = M_{\rm He}, \alpha_{th} = 1) \quad . \tag{2}$$

Fig. 4 shows the evolution of this integrated envelope binding energy as a function of the outer radius. Each panel shows one of our binaries, from top to bottom: $36{+}30\,M_\odot$, $20{+}17\,M_\odot$, $18{+}15\,M_\odot$. For each binary, the lower panel shows the ratios of the envelope binding energy of the accretor divided the binding energy of the comparison single star (i.e., the ratio of the solid lines to

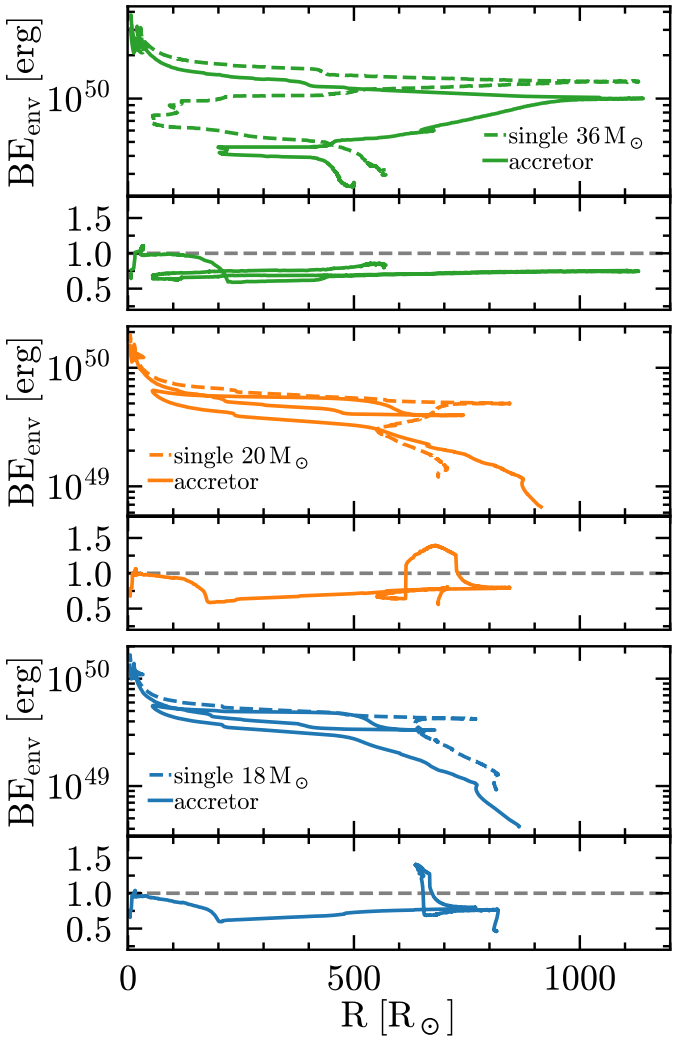

Figure 4. Evolution as a function of the photospheric radius R of the binding energy (including the thermal energy, $\alpha_{\rm th} = 1$) of the accretors and single stars of the same (post-RLOF) total mass. The dashed lines correspond to single stars with the same total mass as the accretors post-RLOF, while solid lines correspond to the accretors. The bottom panels show the ratio, which is always smaller than 1 the first time a certain radius R is reached, indicating that the accretors might have envelopes easier to unbind in a common envelope event. See Fig. 8 for the radial profile at given outer radii R.

the dashed lines in the panel above). To compute these ratios, we interpolate our accretor models on the adaptive time-grid of the single stars using the central temperature $\log_{10}(T_c/[\rm K])$ as independent coordinate. In each of the lower panels the ratios are lower than one (marked by the gray dashed lines) at almost all radii, again suggesting that post-RLOF, accretor stars have envelopes that require less energy input to be ejected in a CE event. The only times the binding energy of the accretor is higher than the corresponding single stars is during the blueward evolution discussed earlier.

4. DISCUSSION & CONCLUSIONS

We have modeled the impact of mass transfer on the envelope structure of the accretor, focusing on thermal timescale, post-donor-main sequence case B RLOF (see Fig. 1). The accretion of mass drives the growth of the accretor's core, changing the core/envelope boundary region and "rejuvenating" the star (Fig. 2). As the accretors evolve beyond the main sequence, they experience large blue-loops which are not expected in single stars of the same mass – with potential implications for asteroseismology (e.g., Dorn-Wallenstein et al. 2020), and the search for non-interacting companions to compact objects (e.g., Breivik et al. 2017; Andrews et al. 2019; Chawla et al. 2021).

The rejuvenation is driven by convective core boundary mixing (e.g., Hellings 1983, 1984; Cantiello et al. 2007; Renzo & Gotberg 2021), and does not occur in its absence (Braun & Langer 1995). The hydrodynamics of convective boundaries in stellar regime is an active topic of research (e.g., Anders et al. 2022a,b), and observations of the width of the main sequence (e.g., Brott et al. 2011) and asteroseismology (e.g., Moravveji et al. 2016) suggest the presence of convective boundary mixing in the core of massive main-sequence stars. In our one-dimensional accretor models, the dominant core boundary mixing is overshooting, with rotationally driven instabilities contributing to a lesser extent during late RLOF. We adopt an exponentially decreasing overshooting diffusion coefficient (Claret & Torres 2017) which may underestimate the amount of mixing at the accretor core boundary. After RLOF, a thick convective shell develops above the core see (see Renzo & Gotberg 2021), which also contributes to the different binding energy profiles (see Fig. 8).

We have focused on the structural consequences of RLOF accretion, specifically their impact on the subsequent binary interaction in the "classical" scenario to a GW merger: the CE event initiated by the RLOF-accretor. Accretors have overall lower binding energy of the envelope (both integrated from the surface to the He core, see Fig. 4 and as a function of radius, see Fig. 3, 8, and 10). The systematically lower binding energy our accretor models compared to single stars of the same outer radius and total mass may imply easier to eject (post-RLOF, second) CE and wider post-CE separations.

Before the onset of the dynamical instability in a CE event, a pre-CE thermal timescale phase of mass transfer may occur (e.g., Hjellming & Webbink 1987;

Pejcha et al. 2017; Blagorodnova et al. 2021). This initial phase is usually neglected in hydrodynamical simulations and may impact the envelope structure of CE-donors whether they have previously been RLOF-accretors (as in our models) or not.

A key uncertainty in CE outcome is the location of the separation between the (possibly) ejected envelope and the remaining core (e.g., Ivanova et al. 2020). This affects equally each CE donor and can have an amplitude comparable to the effect of rejuvenation in accretors (see Fig. 8 for three possible definition of "core"). In the case of rejuvenated CE donors, uncertainty in the core definition compound with the effect of rejuvenation itself.

Not all binary architectures necessarily result in rejuvenated accretors like the ones described here. Very massive BH progenitors ($M_{\rm ZAMS} \gtrsim 40\,M_\odot$) may not expand as red supergiants at all or avoid unstable mass transfer (e.g., van Son et al. 2021; Marchant et al. 2021). Since their main-sequence lifetimes are roughly independent of mass ($\sim 2.5 - 3\,$Myr), at the first RLOF, accretors this massive may already have a deep core/envelope chemical gradient to prevent rejuvenation. However, more massive stars are generally easier to mix (including reaching rotationally-induced chemically homogeneous evolution, e.g., Yoon & Langer 2005; de Mink & Mandel 2016). Shorter initial periods (i.e., earlier mass transfer) and more equal mass ratios can also result in the accretor avoiding the red supergiant phase even at lower masses (Cantiello et al. 2007).

We have focused accretor models for progenitors of NS and BH. However, the physical processes described should be similar in all accretor stars with convective main sequence cores, down to initial mass $M_{\rm ZAMS} \gtrsim 1.2\,M_\odot$ (see also Wang et al. 2020b). Thus, also a fraction of white dwarf progenitor binary systems, if sufficiently massive and experiencing a (case B) RLOF phase of evolution, may be influenced by the structural differences between single stars and RLOF-accretors.

Including the structural reaction to accretion during RLOF in population synthesis simulations could impact the distribution of post-CE orbital separations, the predicted number of "reverse" stellar mergers (e.g., Zapartas et al. 2017), and the rate of GW mergers. Our grid consists only of three binaries, but could be extended to inform semi-analytic approximations of the binding energy of CE-donor that have accreted mass in a previous stable mass transfer phase (see also Fig. 10).

Software: MESA (Paxton et al. 2011, 2015, 2018, 2019), pyMESA (Farmer & Bauer 2018), compare_workdir_MESA[2], Ipython (Perez & Granger 2007), numpy (van der Walt et al. 2011), scipy (Virtanen et al. 2020), matplotlib (Hunter 2007), showyourwork (Luger et al. 2021).

[2] https://github.com/mathren/compare_workdir_MESA/releases/tag/2.0

REFERENCES

Anders, E. H., Jermyn, A. S., Lecoanet, D., & Brown, B. P. 2022a, ApJ, 926, 169, doi: 10.3847/1538-4357/ac408d

Anders, E. H., Jermyn, A. S., Lecoanet, D., et al. 2022b, ApJL, 928, L10, doi: 10.3847/2041-8213/ac5cb5

Andrews, J. J., Breivik, K., & Chatterjee, S. 2019, ApJ, 886, 68, doi: 10.3847/1538-4357/ab441f

Belczynski, K., Holz, D. E., Bulik, T., & O'shaughnessy, R. 2016, Nature, 534, 512, doi: 10.1038/nature18322

Blaauw, A. 1961, \bain, 15, 265

—. 1993, 1, doi: 10.1017/CBO9781107415324.004

Blagorodnova, N., Klencki, J., Vreeswijk, P. M., et al. 2021. https://arxiv.org/abs/2102.05662v1

Brandt, N., & Podsiadlowski, P. 1995, \mnras, 274, 461, doi: 10.1093/mnras/274.2.461

Braun, H., & Langer, N. 1995, A&A, 297, 483

Breivik, K., Chatterjee, S., & Larson, S. L. 2017, ApJL, 850, L13, doi: 10.3847/2041-8213/aa97d5

Broekgaarden, F. S., & Berger, E. 2021, ApJL, 920, L13, doi: 10.3847/2041-8213/ac2832

Brott, I., de Mink, S. E., Cantiello, M., et al. 2011, A&A, 530, A115, doi: 10.1051/0004-6361/201016113

Cantiello, M., Yoon, S., Langer, N., & Livio, M. 2007, A&A, 465, L29

Chawla, C., Chatterjee, S., Breivik, K., et al. 2021, arXiv e-prints, arXiv:2110.05979. https://arxiv.org/abs/2110.05979

Claret, A., & Torres, G. 2017, ApJ, 849, 18, doi: 10.3847/1538-4357/aa8770

de Kool, M. 1990, ApJ, 358, 189, doi: 10.1086/168974

De Marco, O., Passy, J.-C., Moe, M., et al. 2011, MNRAS, 411, 2277, doi: 10.1111/j.1365-2966.2010.17891.x

de Mink, S. E., & Mandel, I. 2016, MNRAS, 460, 3545, doi: 10.1093/mnras/stw1219

Dewi, J. D. M., & Tauris, T. M. 2000, A&A, 360, 1043

Dominik, M., Belczynski, K., Fryer, C., et al. 2012, ApJ, 759, 52, doi: 10.1088/0004-637X/759/1/52

Dorn-Wallenstein, T. Z., Levesque, E. M., Neugent, K. F., et al. 2020, ApJ, 902, 24, doi: 10.3847/1538-4357/abb318

Eggleton, P. P. 1983, ApJ, 268, 368, doi: 10.1086/160960
El-Badry, K., Seeburger, R., Jayasinghe, T., et al. 2022, arXiv:2203.06348 [astro-ph]. https://arxiv.org/abs/2203.06348
Farmer, R., & Bauer, E. B. 2018, pyMesa, doi: 10.5281/zenodo.1205271
Farmer, R., Fields, C. E., Petermann, I., et al. 2016, ApJS, 227, 22, doi: 10.3847/1538-4365/227/2/22
Farmer, R., Renzo, M., de Mink, S. E., Marchant, P., & Justham, S. 2019, The Astrophysical Journal, 887, 53, doi: 10.3847/1538-4357/ab518b
Farrell, E., Groh, J. H., Meynet, G., & Eldridge, J. J. 2022, MNRAS, 512, 4116, doi: 10.1093/mnras/stac538
Fragos, T., Andrews, J. J., Bavera, S. S., et al. 2022, arXiv e-prints, arXiv:2202.05892. https://arxiv.org/abs/2202.05892
Fryer, C. L., Belczynski, K., Wiktorowicz, G., et al. 2012, The Astrophysical Journal, 749, 91, doi: 10.1088/0004-637X/749/1/91
Fryer, C. L., Olejak, A., & Belczynski, K. 2022, arXiv e-prints, arXiv:2204.13025. https://arxiv.org/abs/2204.13025
Gagnier, D., Rieutord, M., Charbonnel, C., Putigny, B., & Espinosa Lara, F. 2019, Astronomy and Astrophysics, 625, 1, doi: 10.1051/0004-6361/201832581
Götberg, Y., de Mink, S. E., & Groh, J. H. 2017, A&A, 608, A11, doi: 10.1051/0004-6361/201730472
Götberg, Y., de Mink, S. E., Groh, J. H., et al. 2018, A&A, 615, A78, doi: 10.1051/0004-6361/201732274
Heger, A., Langer, N., & Woosley, S. E. 2000, ApJ, 528, 368
Hellings. 1983, 369, 1689, doi: 10.1017/CBO9781107415324.004
—. 1984, 1689, doi: 10.1017/CBO9781107415324.004
Hirai, R., Podsiadlowski, P., & Yamada, S. 2018, The Astrophysical Journal, 864, 119, doi: 10.3847/1538-4357/aad6a0
Hjellming, M. S., & Webbink, R. F. 1987, ApJ, 318, 794, doi: 10.1086/165412
Hunter, J. D. 2007, Computing in Science and Engineering, 9, 90, doi: 10.1109/MCSE.2007.55
Hurley, J. R., Tout, C. A., & Pols, O. R. 2002, MNRAS, 329, 897, doi: 10.1046/j.1365-8711.2002.05038.x
Ivanova, N., Justham, S., & Ricker, P. 2020, Common Envelope Evolution, 2514-3433 (IOP Publishing), doi: 10.1088/2514-3433/abb6f0
Ivanova, N., Justham, S., & Ricker, P. 2020, Common Envelope Evolution, doi: 10.1088/2514-3433/abb6f0
Ivanova, N., Justham, S., Chen, X., et al. 2013, The Astronomy and Astrophysics Review, 21, 59, doi: 10.1007/s00159-013-0059-2
Kalogera, V. 1996, \apj, 471, 352, doi: 10.1086/177974
Kippenhahn, R., & Weigert, A. 1967, ZA, 65, 251
Klencki, J., Istrate, A. G., Nelemans, G., & Pols, O. 2021. https://arxiv.org/abs/2111.10271
Klencki, J., Nelemans, G., Istrate, A. G., & Chruslinska, M. 2020. https://arxiv.org/abs/2006.11286
Korol, V., Rossi, E. M., Groot, P. J., et al. 2017, Monthly Notices of the Royal Astronomical Society, 470, 1894, doi: 10.1093/mnras/stx1285
Kremer, K., Breivik, K., Larson, S. L., & Kalogera, V. 2017, ApJ, 846, 95, doi: 10.3847/1538-4357/aa8557
Kruckow, M. U., Tauris, T. M., Langer, N., Kramer, M., & Izzard, R. G. 2018, MNRAS, 481, 1908, doi: 10.1093/mnras/sty2190
Langer, N. 1998, Astronomy and Astrophysics, 329, 551
Laplace, E., Götberg, Y., De Mink, S. E., Justham, S., & Farmer, R. 2020, Astronomy and Astrophysics, 637, A6, doi: 10.1051/0004-6361/201937300
Laplace, E., Justham, S., Renzo, M., et al. 2021, A&A, 656, A58, doi: 10.1051/0004-6361/202140506
Lau, M. Y. M., Hirai, R., González-Bolívar, M., et al. 2022, MNRAS, doi: 10.1093/mnras/stac049
Law-Smith, J. A. P., Everson, R. W., Ramirez-Ruiz, E., et al. 2020, arXiv e-prints, arXiv:2011.06630. https://arxiv.org/abs/2011.06630
Lubow, S. H., & Shu, F. H. 1975, ApJ, 198, 383, doi: 10.1086/153614
Luger, R., Bedell, M., Foreman-Mackey, D., et al. 2021, arXiv e-prints, arXiv:2110.06271. https://arxiv.org/abs/2110.06271
Maeder, A., & Meynet, G. 2000, ARA&A, 38, 143, doi: 10.1146/annurev.astro.38.1.143
Marchant, P., Pappas, K. M. W., Gallegos-Garcia, M., et al. 2021, doi: 10.1051/0004-6361/202039992
Moravveji, E., Townsend, R. H. D., Aerts, C., & Mathis, S. 2016, ApJ, 823, 130, doi: 10.3847/0004-637X/823/2/130
Müller, P. E., & Vink, J. S. 2014, Astronomy and Astrophysics, 564, 1, doi: 10.1051/0004-6361/201323031
Neo, S., Miyaji, S., Nomoto, K., & Sugimoto, D. 1977, \pasj, 29, 249
O'Connor, E., & Ott, C. D. 2011, ApJ, 730, 70
Ogata, M., Hirai, R., & Hijikawa, K. 2021, 14, 1. https://arxiv.org/abs/2103.10111
Packet, W. 1981, A&A, 1, doi: 10.1017/CBO9781107415324.004
Paczyński, B. 1971, ARA&A, 9, 183, doi: 10.1146/annurev.aa.09.090171.001151
Paczynski, B. 1976, in Structure and Evolution of Close Binary Systems, ed. P. Eggleton, S. Mitton, & J. Whelan, Vol. 73, 75

Patton, R. A., & Sukhbold, T. 2020, MNRAS, 499, 2803, doi: 10.1093/mnras/staa3029
Patton, R. A., Sukhbold, T., & Eldridge, J. J. 2021, 11, 1. https://arxiv.org/abs/2106.05978
Patton, R. A., Sukhbold, T., & Eldridge, J. J. 2022, MNRAS, 511, 903, doi: 10.1093/mnras/stab3797
Pavlovskii, K., Ivanova, N., Belczynski, K., & Van, K. X. 2017, Monthly Notices of the Royal Astronomical Society, 465, 2092, doi: 10.1093/mnras/stw2786
Paxton, B., Bildsten, L., Dotter, A., et al. 2011, ApJS, 192, 3, doi: 10.1088/0067-0049/192/1/3
Paxton, B., Cantiello, M., Arras, P., et al. 2013, ApJS, 208, 4, doi: 10.1088/0067-0049/208/1/4
Paxton, B., Marchant, P., Schwab, J., et al. 2015, ApJS, 220, 15, doi: 10.1088/0067-0049/220/1/15
Paxton, B., Schwab, J., Bauer, E. B., et al. 2018, ApJS, 234, 34, doi: 10.3847/1538-4365/aaa5a8
Paxton, B., Smolec, R., Gautschy, A., et al. 2019. https://arxiv.org/abs/1903.01426
Pejcha, O., Metzger, B. D., Tyles, J. G., & Tomida, K. 2017, ApJ, 850, 59, doi: 10.3847/1538-4357/aa95b9
Perez, F., & Granger, B. E. 2007, Computing in Science Engineering, 9, 21, doi: 10.1109/MCSE.2007.53
Ramírez-Agudelo, O. H., Sana, H., de Mink, S. E., et al. 2015, A&A, 580, A92, doi: 10.1051/0004-6361/201425424
Renzo, M., Farmer, R. J., Justham, S., Mink, S. E. D., & Marchant, P. 2020, Monthly Notices of the Royal Astronomical Society, 4341, 4333, doi: 10.1093/mnras/staa549
Renzo, M., & Gotberg, Y. 2021, arXiv e-prints, arXiv:2107.10933. https://arxiv.org/abs/2107.10933
Renzo, M., Hendriks, D. D., van Son, L. A. C., & Farmer, R. 2022, arXiv:2201.10519 [astro-ph]. https://arxiv.org/abs/2201.10519
Renzo, M., Ott, C., Shore, S., & De Mink, S. 2017, Astronomy and Astrophysics, 603, doi: 10.1051/0004-6361/201730698
Renzo, M., Zapartas, E., de Mink, S. E., et al. 2019, Astronomy & Astrophysics, 66, 1, doi: 10.1051/0004-6361/201833297
Renzo, M., Callister, T., Chatziioannou, K., et al. 2021, ApJ, 919, 128, doi: 10.3847/1538-4357/ac1110
Sen, K., Langer, N., Marchant, P., et al. 2022, A&A, 659, A98, doi: 10.1051/0004-6361/202142574
Sravan, N., Marchant, P., & Kalogera, V. 2019, The Astrophysical Journal, 885, 130, doi: 10.3847/1538-4357/ab4ad7
Tauris, T. M., & Takens, R. J. 1998, Astronomy and Astrophysics, 1059, 1047
Tauris, T. M., Kramer, M., Freire, P. C. C., et al. 2017, ApJ, 846, 170, doi: 10.3847/1538-4357/aa7e89
Thiele, S., Breivik, K., & Sanderson, R. E. 2021, arXiv e-prints, arXiv:2111.13700. https://arxiv.org/abs/2111.13700
Tutukov, A. V., & Yungelson, L. R. 1993, MNRAS, 260, 675, doi: 10.1093/mnras/260.3.675
van den Heuvel, E. P. J., Portegies Zwart, S. F., & de Mink, S. E. 2017, MNRAS, 471, 4256, doi: 10.1093/mnras/stx1430
van der Walt, S., Colbert, S. C., & Varoquaux, G. 2011, Computing in Science and Engineering, 13, 22, doi: 10.1109/MCSE.2011.37
van Son, L., de Mink, S., Callister, T., et al. 2021, arXiv e-prints, arXiv:2110.01634. https://arxiv.org/abs/2110.01634
Vigna-Gómez, A., Neijssel, C. J., Stevenson, S., et al. 2018, Monthly Notices of the Royal Astronomical Society, 481, 4009, doi: 10.1093/mnras/sty2463
Vigna-Gómez, A., MacLeod, M., Neijssel, C. J., et al. 2020, PASA, 37, e038, doi: 10.1017/pasa.2020.31
Virtanen, P., Gommers, R., Oliphant, T. E., et al. 2020, Nature Methods, 17, 261, doi: 10.1038/s41592-019-0686-2
Walmswell, J., Tout, C. A., & Eldridge, J. J. 2015, \mnras, 447, 2951, doi: 10.1093/mnras/stu2666
Wang, C., Langer, N., Schootemeijer, A., et al. 2020a, ApJL, 888, L12, doi: 10.3847/2041-8213/ab6171
—. 2020b, ApJL, 888, L12, doi: 10.3847/2041-8213/ab6171
Wang, L., Gies, D. R., Peters, G. J., et al. 2021. https://arxiv.org/abs/2103.13642
Webbink, R. F. 1984, ApJ, 277, 355, doi: 10.1086/161701
Yoon, S.-C. 2017, MNRAS, 470, 3970, doi: 10.1093/mnras/stx1496
Yoon, S. C., & Langer, N. 2005, A&A, 443, 643, doi: 10.1051/0004-6361:20054030
Zapartas, E., de Mink, S. E., Izzard, R. G., et al. 2017, A&A, 601, A29, doi: 10.1051/0004-6361/201629685
Zapartas, E., Renzo, M., Fragos, T., et al. 2021, A&A, 656, L19, doi: 10.1051/0004-6361/202141506
Zorotovic, M., Schreiber, M. R., Gänsicke, B. T., & Nebot Gómez-Morán, A. 2010, A&A, 520, A86, doi: 10.1051/0004-6361/200913658

APPENDIX

A. IMPACT OF CORE-ENVELOPE BOUNDARY AND ROTATION ON THE BINDING ENERGY PROFILE

In this appendix, we introduce our "engineered" models and illustrate with examples how the envelope binding energy depends on the CEB layer (Sec. A.1) and on the initial rotation rate of the star (Sec. A.2). Both can be significantly modified by accretion during the first RLOF.

Fig. 5 shows an example grid of "engineered stars" of $30 M_\odot$, similar to Fig. 2. Starting from a non-rotating single star at TAMS (e.g., red model in Fig. 5), we modify the CEB specific entropy (s) which controls the thermal properties of the gas, and its H, and He profiles – but do not change the mass fractions of other elements. Specifically, we keep the same inner and outer profiles, but impose a linear connection from the outer boundary of the H-depleted core to a mass coordinate which we specify as a parameter (see Fig. 5 and Fig. 2). We let `MESA` relax the TAMS profiles to the desired entropy and composition profiles and then recover thermal and hydrostatic equilibrium, and then evolve until either carbon depletion or when the photospheric radius of these models first exceeds $1000\,R_\odot$.

A.1. *Steepness of the core-envelope boundary*

Fig. 6 shows a comparison of the gravitational and binding energy profiles of a $30\,M_\odot$ single star (red solid line) to "engineered" models, when stars first reach radius $R = 500\,R_\odot$. Fig. 6 shows that binding energy depends on the structure of the CEB region. In single stars, the CEB is determined by the extent of the convective boundary mixing and the recession in mass coordinate of the convective core. In Fig. 6, lines of different colors show a trend with shallower entropy and composition profiles at TAMS (lighter curves in Fig. 6) evolving into more bound inner envelopes (larger binding energy inside $\log_{10}(r/\mathrm{cm}) \lesssim 11.5$), and viceversa.

A.2. *Rotation*

Mass transfer through RLOF from a binary companion also spins up the accreting star, often to critical rotation[3] (e.g., Lubow & Shu 1975; Packet 1981; Cantiello et al. 2007). Although spinning up a star late during its main-sequence evolution has a different structural consequences than natal rotation (see Renzo & Gotberg 2021), our accretor models can reach a rigid, close-to-critical rotation late during RLOF. Thus, it is worth considering the impact of rotation on the envelope structure and CEB by analyzing single star models rotating since birth.

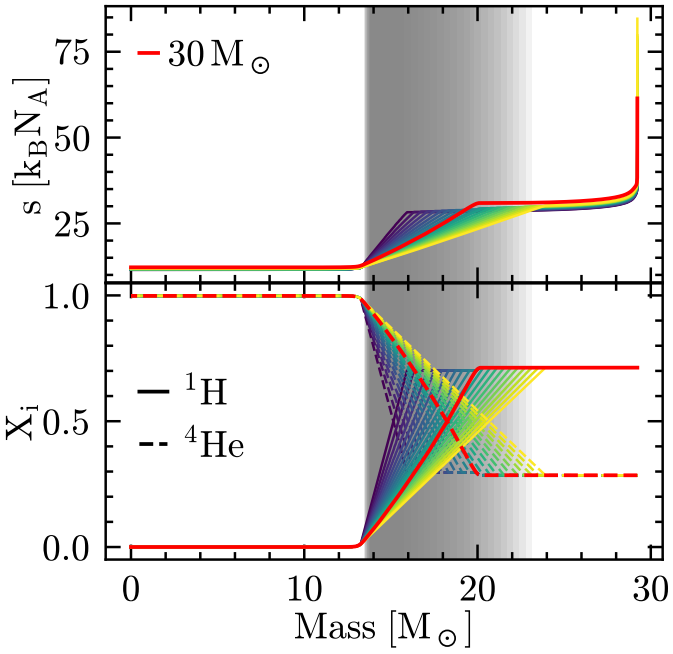

Figure 5. TAMS entropy profile of a single $30\,M_\odot$ star (red) and engineered models where we artificially modify the CEB region (gray shaded area partially overlapping for multiple models). The CEB for a single $30\,M_\odot$ star has a mass thickness of $5.81\,M_\odot$ at TAMS, while the engineered models span the range $\sim 3 - 9.4\,M_\odot$.

Rotation has a two main effects: (i) mixing can change the core size directly (see Heger et al. 2000; Maeder & Meynet 2000), (ii) changes in the mass-loss rate (e.g., Langer 1998; Müller & Vink 2014; Gagnier et al. 2019) affect the rate of recession of the convective core (e.g., Renzo et al. 2017, 2020). By inflating the equatorial region, rotation changes the temperature and opacity structure, and therefore the line-driving of the wind. Moreover, rotation can have a dynamical effect, resulting in mass loss through the combination of centrifugal forces and radiative pressure ($\Gamma - \Omega$ limit, Langer 1998). One-dimensional stellar evolution codes commonly assume that rotation increases the total mass loss rate (e.g., Langer 1998; Heger et al. 2000) though this may

[3] At critical rotation, the centrifugal force balances the gravitational pull at the equator, corresponding to angular frequency $\omega_{\rm crit} = \sqrt{(1 - L/L_{\rm Edd})GM/R^3}$ is the critical spin frequency, with $L_{\rm Edd}$ the Eddington luminosity, and L is the luminosity.

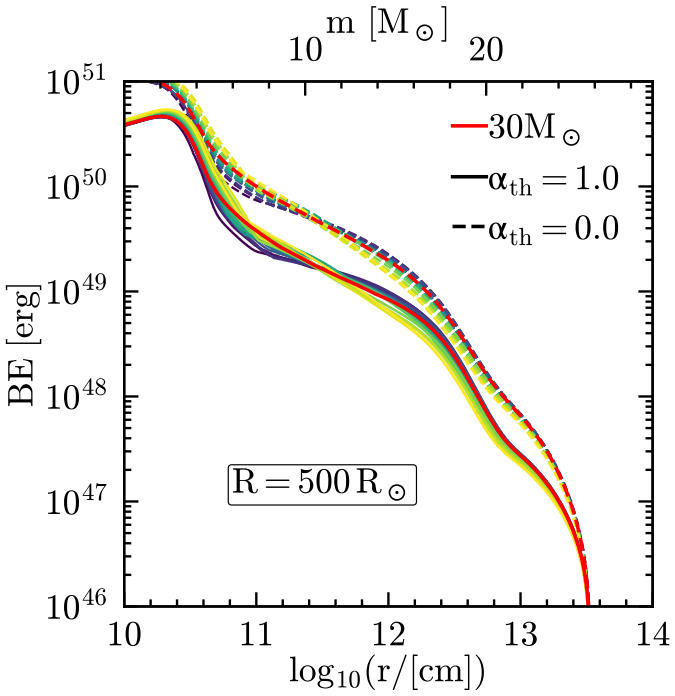

Figure 6. The structure of the CEB at the end of the main sequence impacts the envelope binding energy profile throughout the remaining evolution. Dashed lines show the gravitational contribution only, while solid lines include the contribution of the internal energy. The red lines show a $30\,M_\odot$, non-rotating, $Z = 0.0019$ model compared to "engineered" models of the same mass (see Fig. 5), but artificially imposed profile at TAMS (other colors, see text). The top (bottom) axis indicates mass coordinate (radius). We compare the models when they first reach $500\,R_\odot$.

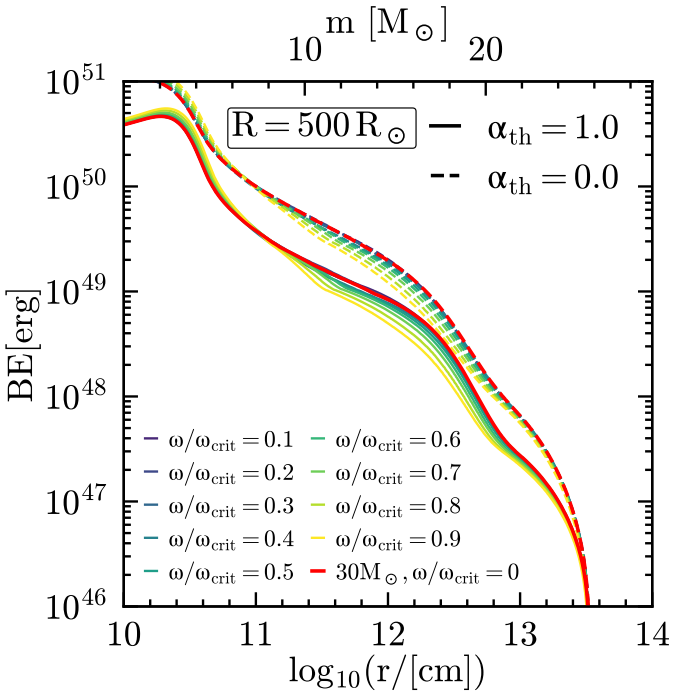

Figure 7. Same as Fig. 6 but comparing single stars differing by their initial rotation rate.

not always be true throughout the evolution (e.g., Gagnier et al. 2019).

Fig. 7 shows the gravitational binding energy profile of the single $30\,M_\odot$ star of Fig. 6, compared to single stars of the same mass and varying initial $\omega/\omega_{\rm crit}$. For $\omega/\omega_{\rm crit} \lesssim 0.5$, corresponding to a generous upper-bound for the typical birth rotation rate of single massive stars (e.g., Ramírez-Agudelo et al. 2015), the effect is modest but non-negligible. For more extreme initial rotation rates (achievable during RLOF, at least in the surface layers), the ratio of the He core mass to total mass is significantly changed by rotational mixing, which can result in larger binding energy differences than changing the CEB layer at fixed core mass.

For stars accreting through RLOF in a binary both effects illustrated in Fig. 6 and Fig. 7 act simultaneously, although the timing and amplitude of the impact of mixing and rotation can be different than for single stars (e.g., Renzo & Gotberg 2021).

B. BINDING ENERGY PROFILES

In Fig. 8, we show the binding energy of our accretor models (solid lines, including the internal energy, i.e. $\alpha_{\rm th} = 1$ in Eq. 1), single stars with initial mass roughly equal to the accretors post-RLOF mass, and our engineered models (see also Fig. 10 for the $\lambda_{\rm CE}$ profile defined in Appendix D). The two lowest mass accretors (left and central column) do not expand to $R = 1000\,R_\odot$ before carbon depletion. Generally speaking, the accretors (orange) have lower binding energies than corresponding single stars (red), and their profiles are qualitatively closer to the engineered models with the steepest core (darker curves), although local deviations from this trend can occur for some r.

C. COMPARISON WITH SAME CORE MASS

Fig. 2 compares our accretor models to stars of the same total *post-RLOF* mass. However, it is not obvious that models of the same total mass are the most relevant comparison: for instance, the (helium or carbon-oxygen) core mass is often used to determine the final compact object (e.g., Fryer et al. 2012; Farmer et al. 2019; Patton et al. 2021; Renzo et al. 2022; Fryer et al. 2022), and comparing models of roughly the same core-mass might be more appropriate (but is sensitive to the condition defining the core edge). We show in Fig. 9 a comparison of our accretors with models of the same total *initial*

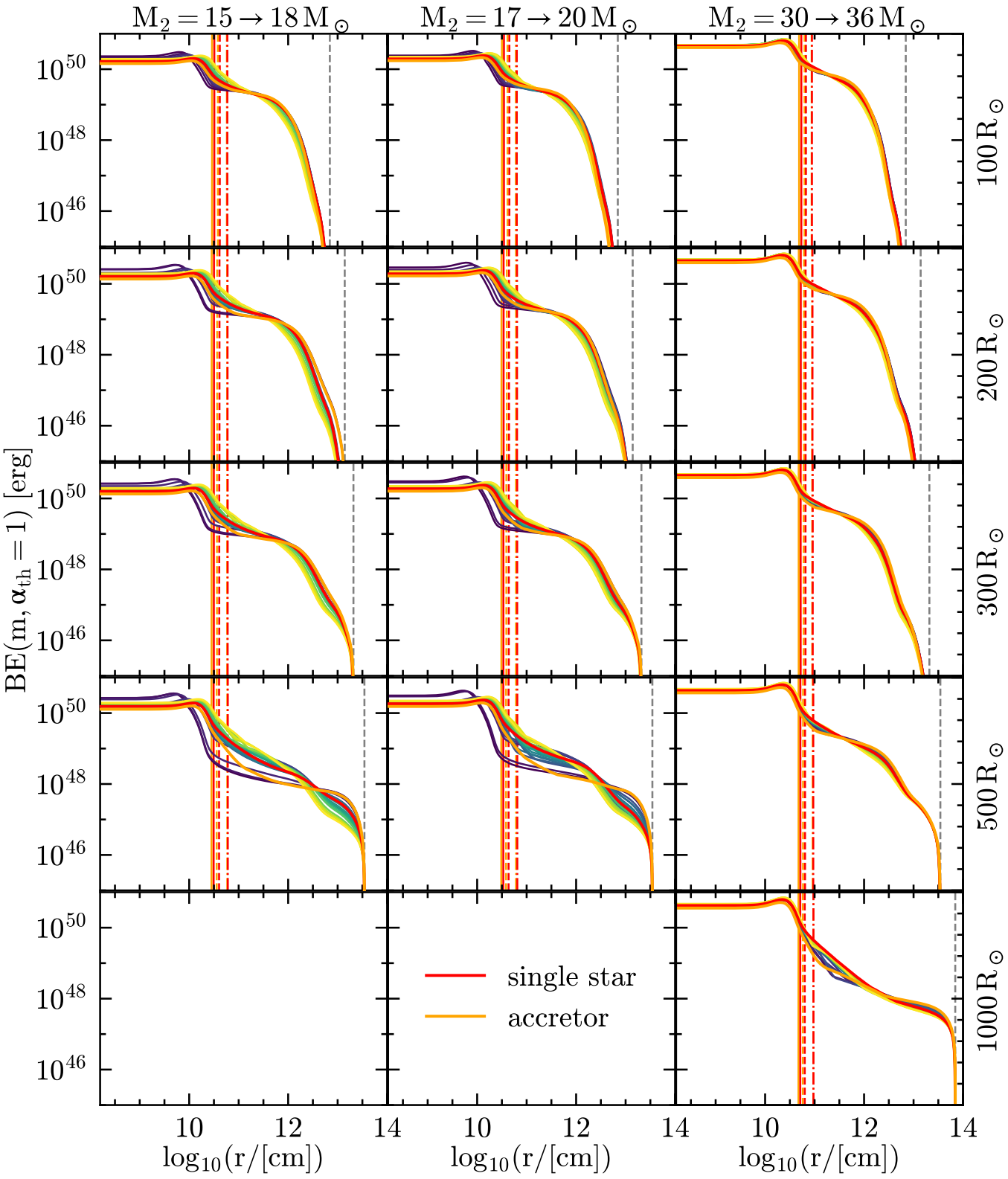

Figure 8. Binding energy profile at fixed photospheric radius R (right y-axis) as a function of radius $r(m)$. We only show profiles with $\alpha_{\rm th} = 1$, that is accounting for the internal energy content of the star. Orange, red, and other colors show respectively the accretor models, single stars of same post-RLOF total mass, and engineered models with varying CEB steepness. Titles indicates the pre-RLOF and approximate post-RLOF accretor masses. The vertical colored lines mark the outer edge of the helium cores of the accretor and single star, that is the outermost location where $Y > 0.1$ and $X < 0.01$ (solid lines), or $X < 0.1$ (dashed), or $X < 0.2$ (dot-dashed). The ggray dashed lines mark the total radius R of these models.

mass, which constitute the extreme opposite comparison point.

D. COMMON ENVELOPE $\lambda_{\rm CE}$

de Kool (1990) introduced a binding energy parameter $\lambda_{\rm CE}$ to account for the internal structure of the stars when calculating the post-CE orbit using energy conservation:

$$\lambda_{\rm CE} \equiv \lambda_{\rm CE}(m) = (GM(M-m)/R)/BE(m, \alpha_{\rm th} = 1.0) \ , \tag{D1}$$

where again the Lagrangian mass coordinate m can be interpreted as a variable core mass (see also De Marco et al. 2011; Ivanova et al. 2013). While de Kool (1990) used $\alpha_{\rm CE} = 0$, we calculate $\lambda_{\rm CE}$ with $\alpha_{\rm CE} = 1.0$, which provides a best case scenario for the ejection of the CE by harvesting the entire internal energy available in the gas. We show in Fig. 10 the $\lambda_{\rm CE}$ profiles for our models.

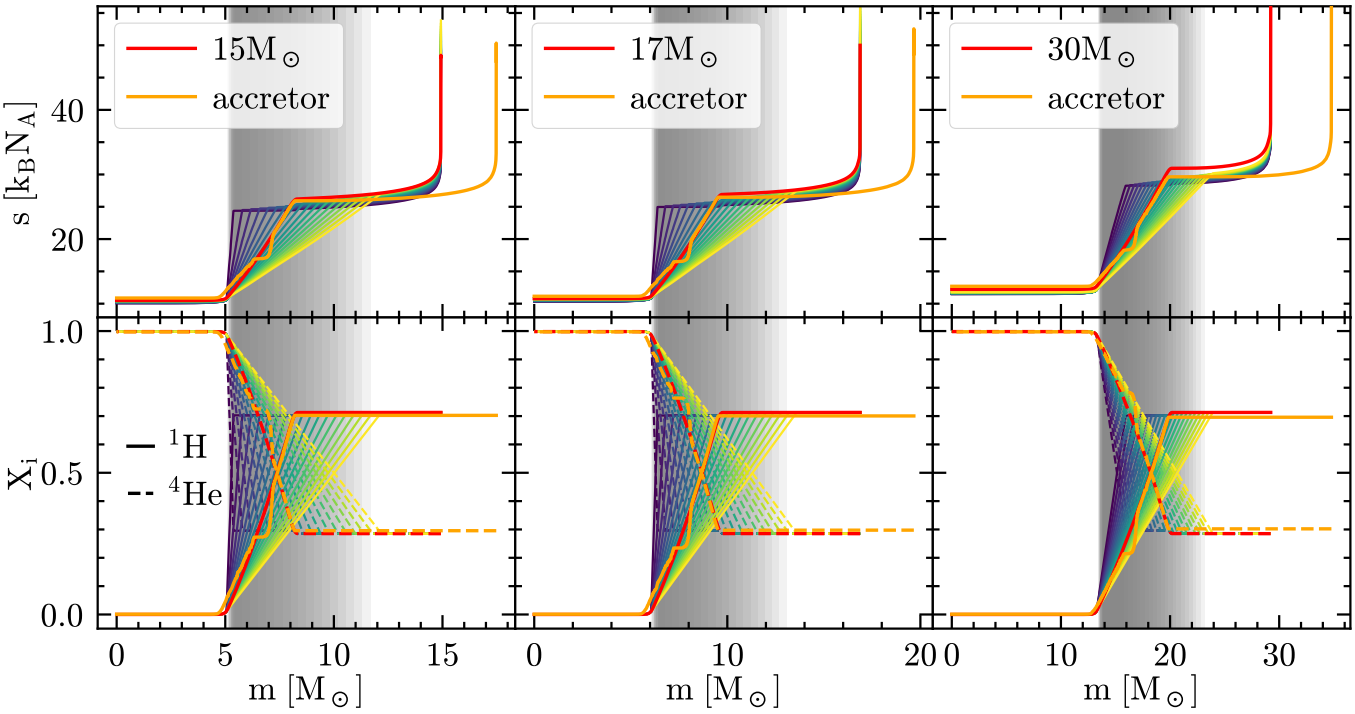

Figure 9. Specific entropy (top row), H (bottom row, solid lines), and He (bottom row, dashed lines) profiles for non-rotating single stars (red), accretors (orange), and "engineered" models of the same total mass as the ZAMS mass of the accretors. The overlapping gray bands emphasize the CEB region.

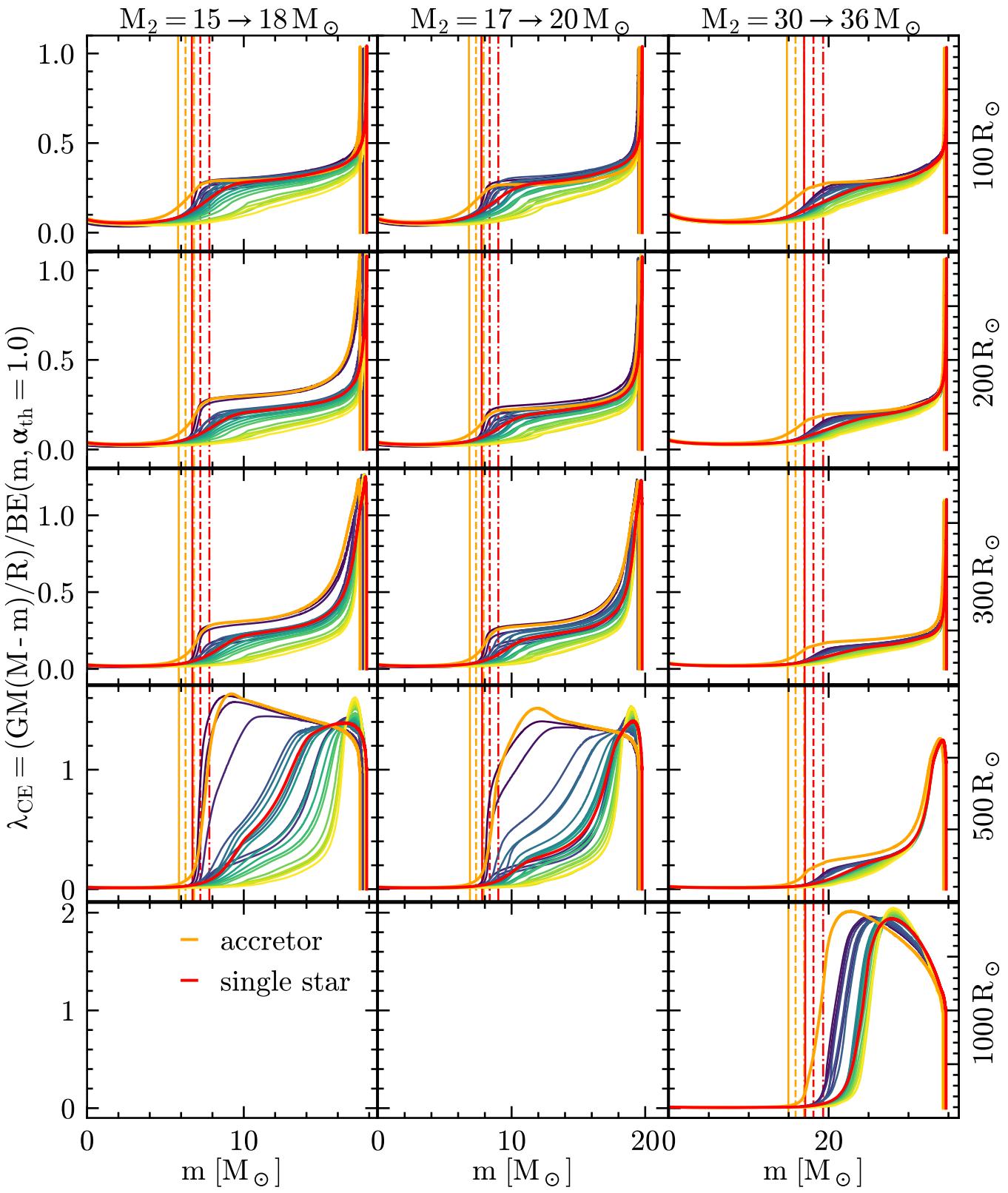

Figure 10. Profile of the binding energy parameter $\lambda_{\rm CE}$ as a function of mass coordinate for accretors (orange), single stars (red), and our engineered stars (other colors) at selected total radii. The vertical lines mark the outer edge of the helium cores of the accretor and single star, that is the outermost location where $Y > 0.1$ and $X < 0.01$ (solid lines), or $X < 0.1$ (dashed), or $X < 0.2$ (dot-dashed).